UNIVERSITY OF CALIFORNIA, LOS ANGELES

MECHANICAL AND AEROSPACE ENGINEERING DEPARTMENT

MAE 154A Final Report
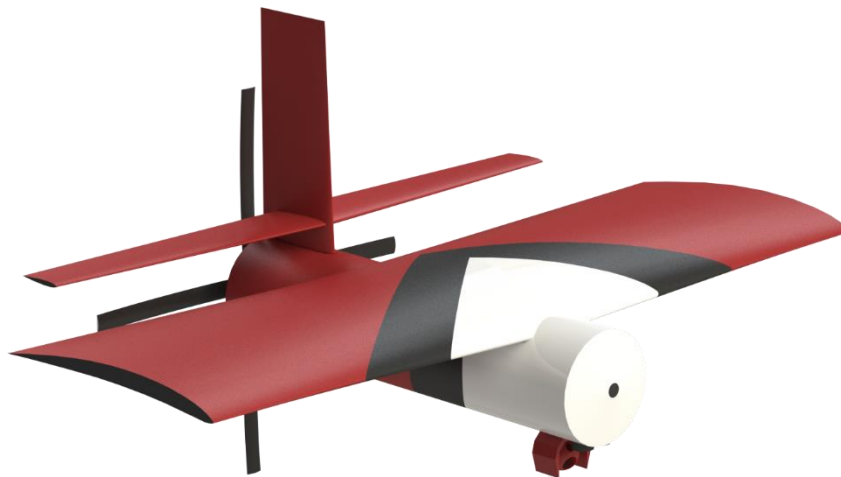
Group 4

Alan McIvor

David Thorne

Thomas Freedman

Willy Teav

Abstract

Increased fires in Southern California have drawn interest from the US Forest Service in deploying semi-permanent UAVs to monitor Angeles National Forest for fires. The USFS requests a drone which will be able to survey all 1024 mi^2 of Angeles National Forest and scan for developing wildfires. A UAV will be cheaper and faster to develop than a satellite, while helping protect the resources of Angeles National Forest and preventing a fire which could disrupt Los Angeles, the largest economic hub in the western United States and home of the UCLA Bruins.

Contents

1. Mission

1.1 Mission Inspiration

Each member of the team is a California resident, familiar with the seasonal threats fires pose across the state. Specifically, the Skirball fire in 2017 cancelled classes at the end of our first quarter at UCLA, giving us first-hand experience of the disruptions a wildfire can have.

With the threat of global warming accelerating the occurrence and severity of wildfires, we wanted to engineer an early warning or detection system for the nearest significant forest, the Angeles National Forest. We narrowed in on detection because of how fast a fire can spread, only taking hours to spread past easy containment.

Thus, a mission designed around area coverage and payload selection allowed for a meaningful and challenging design. Our challenge was to be cheaper than a satellite, and have quicker detection than existing systems, requiring pseudo constant observation from a high altitude.

1.2 Mission Requirements

The determined mission requirements are listed in Table 1 below.

Table 1: UAV Design Requirements

Requirement	Target	Design	Delta
Endurance	3 days	3.1651 days	5.5%
Coverage	1024 mi^2/day	1024 mi^2/day	0%
Mass	minimize	1107 lbs	-

The endurance requirement reflects the client desire for semi-permanent surveillance. A small fleet of two UAVs could maintain constant coverage, with a possible third for maintenance periods. The coverage requirement is derived from the area of Angeles National Forest, which is roughly 1024 sq mi. The UAV was optimized to minimize mass, as it is tied to many other drawdown specs such as cost and maintenance.

1.3 Payload

Two payload sensors were chosen. The first is a thermal imager designed for low-Earth orbit satellites which would be able to detect hot spots where fires may be forming from a high altitude. Because the sensor is designed for cubesats, it is low power and very high resolution, ideal for this mission. The second sensor is a more traditional gimballed camera which would allow our UAV to send visual updates on a developing fire that it covers. The two payload sensors are seen in Figure 1 below.

Figure 1:EPSILON 140 (visual) (left), and SATLANTIS ISIM-90 (thermal) (right).

One key specification from the SATLANTIS is the swath width. The given specification is that is has a swath of 13km at an altitude of 500km. This geometry was maintained to give a relationship between the cruise velocity and altitude. Using the coverage requirement and swath width as a function of altitude, we found the relationship between altitude and velocity to be linked by equation 1.

$$Altitude = \frac{8.66 \times 10^6}{Velocity} \tag{1}$$

2. Primary Design

2.1 Relevant Aircraft Survey

In designing this aircraft based on the specified mission (persistent surveillance), pre-existing aircraft with a similar mission profile were referenced. These included the Lockheed U-2, Airbus Zephyr, Scaled Composites Proteus, and Rutan Voyager. Notably, all except the Zephyr from these examples are manned aircraft, while ours was unmanned.

The majority of aircraft consulted were used for weight/sizing estimates, while the U-2 in particular was used to estimate the fuel weight as a percentage of gross weight. A table of the aircraft consulted for this effort is seen below, along with relevant specifications for each example.

Table 2: Relevant Aircraft Survey and Specifications

Aircraft	VANILLA VA001 Group 3 UAS	MQ-1C Gray Eagle (Extended Range)	MQ-9B	Predator XP	RQ-4
Max Altitude (ft)	15,000	29,000	40,000	25,000	60,000
Speed (mph)	86 (max)	192 (max)	242 (max)	138 (avg)	357 (--)
Endurance (days)	10+	~2 (just under)	~2 (just under)	~1.5	~1.5
Range (mi)	--	2877	--	--	14,155
Max Takeoff Weight (lbs)	--	4,200	12,500	2,550	32,250
Empty Weight (lbs)	475	--	--	--	14,950
Plane Length (ft)	--	28	38	27	47.6

Wing Span (ft)	36	58	79	55	130.9
Payload Capacity (lbs)	50	900	4,800	--	3,000
Powerplant	--	HFE-180HP heavy-fuel engine	Honeywell TPE331-10 Turboprop	Heavily Modified Rotax 914 Turbo	RR F137-RR-100 turbofan
Fuel Capacity (lbs)	--	900	6,000	595	17,300
Notes	towed takeoff	max range achieved with satellite comms. inverted v-tail. high aspect ratio. no winglets	v-tail. high aspect ratio. winglets. retractable landing gear.	inverted v-tail. high aspect ratio. winglets. retractable landing gear.	v-tail. high aspect ratio. no winglets. retractable landing gear.

2.2 Final Design Specifications

The final design inputs are listed in Table 3, and the final design SOLIDWORKS model shown in Figure 2 below.

Table 3: Aircraft Final Specifications

Aircraft Length	10 ft
Wingspan	21.45 ft
Wing Aspect Ratio	3.07
Aileron Effectiveness Parameter	0.4604
Propeller Blades	4

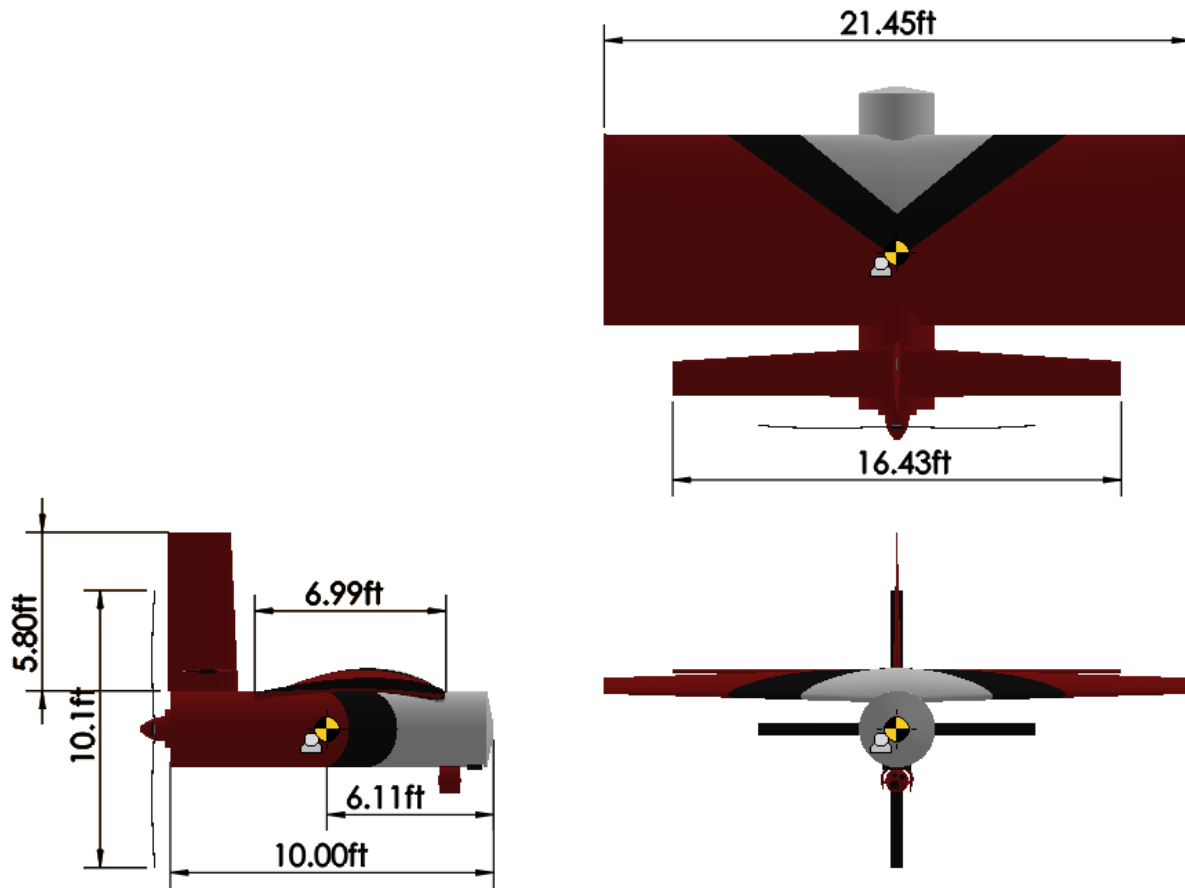|	
Propeller Diameter	10.1 ft
Propeller Efficiency	0.85
Blade Angle	20°
Engine Weight	132.3 lbs
Engine Power	80 hp
Engine Specific Fuel Consumption	$0.469 \; {lbs}/{(hp-hr)}$
Center of Gravity Location (Loaded)	6.11 ft
Center of Gravity Location (Unloaded)	5.63 ft
Static Margin (Loaded)	0.564
Static Margin (Unloaded)	0.657
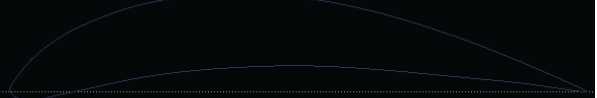
Figure 2: Final SOLIDWORKS Model 3-View
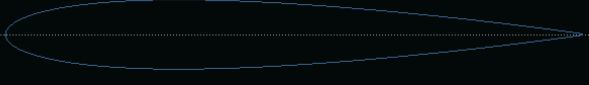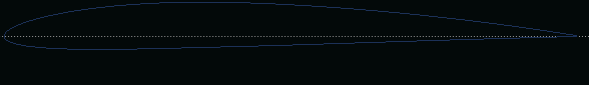
3. Aerodynamics

3.1 Airfoil Options/ Selection

The initial airfoil candidates were taken by searching the AirfoilTools database for airfoils with the maximum C_L/C_D ratios over a range of different Reynolds numbers. In addition, several more high C_L/C_D 4-digit NACA airfoils and a popular generic airfoil were selected as wildcards since they are heavily standardized and therefore easier to work with. The airfoil candidates were all cambered but varied drastically in shape and thickness. A symmetric airfoil (NACA 0012) was thrown into the mix to have an airfoil that is appropriate for stabilizers.

9

Table 4: Airfoil Candidates

Airfoil	Image	Selection Reason
AG25 Bubble Dancer	AG25 Bubble Dancer DLG by Mark Drela Thickness = 7.58% Max. Thick.pos. = 25.53% Max. Camber = 2.40% Max. Camber pos. = 45.55%	Popular Airfoil
Davis Basic B-24 Wing Airfoil	DAVIS BASIC B-24 WING AIRFOIL Thickness = 15.90% Max. Thick.pos. = 29.22% Max. Camber = 2.48% Max. Camber pos. = 29.22%	High C_L/C_D at Re = 2e6 and 5e6
E63	E63 (4.25%) Thickness = 4.27% Max. Thick.pos. = 22.95% Max. Camber = 5.39% Max. Camber pos. = 51.77%	High C_L/C_D at Re =5e5
Eppler 376	EPPLER 376 AIRFOIL Thickness = 2.45% Max. Thick.pos. = 5.19% Max. Camber = 8.93% Max. Camber pos. = 33.12%	High C_L/C_D at Re =1e5
Eppler 58	EPPLER 58 AIRFOIL Thickness = 5.62% Max. Thick.pos. = 22.80% Max. Camber = 6.46% Max. Camber pos. = 52.14%	High C_L/C_D at Re =1e6
GOE 448	GOE 448 AIRFOIL Thickness = 12.92% Max. Thick.pos. = 33.10% Max. Camber = 10.55% Max. Camber pos. = 43.42%	High C_L/C_D at Re = 2e6
GOE 79	GOE 79 (PFALZ 11) AIRFOIL Thickness = 6.21% Max. Thick.pos. = 16.77% Max. Camber = 6.02% Max. Camber pos. = 33.79%	High C_L/C_D at Re = 5e5

NACA 0012	NACA 0012 Thickness = 12.00% Max. Thick.pos. = 30.84% Max. Camber = 0.15% Max. Camber pos. = 0.01%	Symmetric Airfoil
NACA 2408	NACA 2408 Thickness = 8.00% Max. Thick.pos. = 30.23% Max. Camber = 2.00% Max. Camber pos. = 39.44%	High NACA C_L/C_D at Re = 5e5
NACA 6409	NACA 6409 Thickness = 9.00% Max. Thick.pos. = 29.14% Max. Camber = 6.00% Max. Camber pos. = 40.65%	High NACA C_L/C_D at Re = 5e5 to 1e6, similar to U2 airfoil

Coordinates were downloaded from AirfoilTools and used to generate airfoil geometry in XFLR5. Each airfoil was repaneled and discretized into 100 sections for consistency. Then, a batch analysis was ran for all of the airfoils at 12 different Reynolds numbers ranging from 30,000 to 3,000,000 and angle of attack varying from -5 to 10 degrees in .5 degree increments. Forced upper and lower transitions were set to 1 as to not introduce any unnatural turbulence generation on the airfoils.

AG25 Bubble Dancer DLG by Mark Drela
      T1_Re0.500_M0.00_N9.0

DAVIS BASIC B-24 WING AIRFOIL
      T1_Re0.500_M0.00_N9.0

E63 (4.25%)
      T1_Re0.500_M0.00_N9.0

EPPLER 58 AIRFOIL
      T1_Re0.500_M0.00_N9.0

GOE 79 (PFALZ 11) AIRFOIL
      T1_Re0.500_M0.00_N9.0

NACA 2408
      T1_Re0.500_M0.00_N9.0

NACA 6409
      T1_Re0.500_M0.00_N9.0
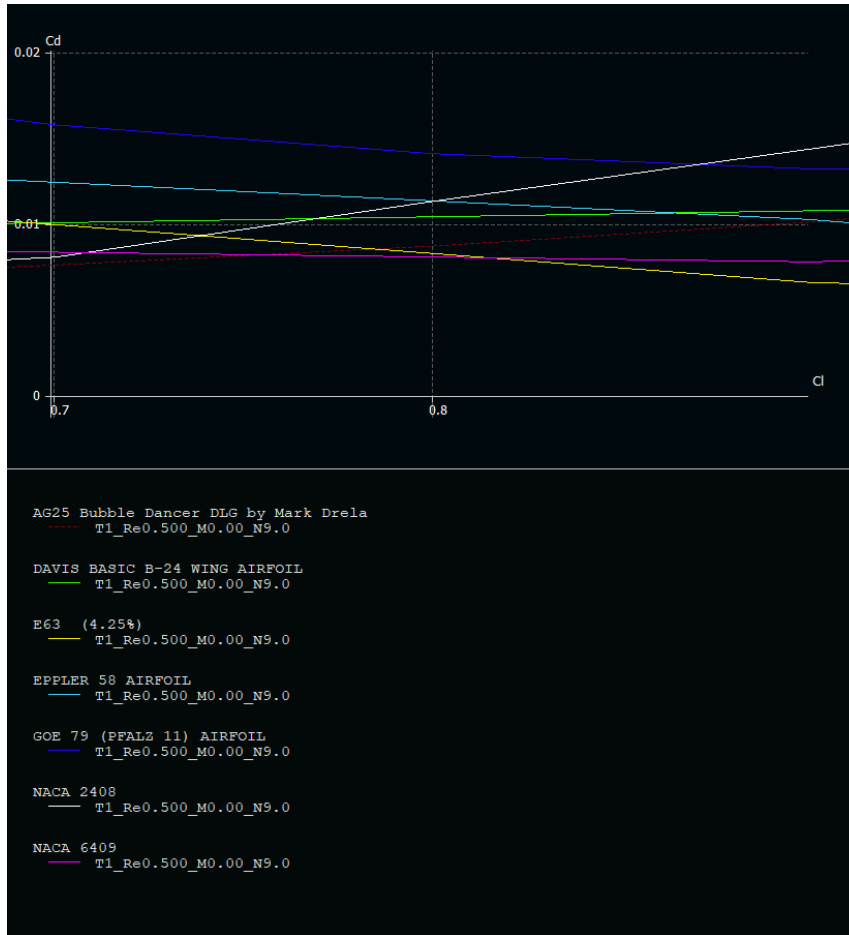
Figure 3: Airfoil C_L vs C_D comparison at $C_L = 0.8$

After the analysis was run, the initial idea was to check which airfoil has the lowest drag at a given design C_L. The main issue with this approach is that the design C_L is arbitrary. The XFLR5 was exported to Excel in preparation for being imported by MATLAB. There was a separate .csv file for each airfoil at each Reynolds number, totaling to 120 different files that needed to be concatenated. The exported data also needed to be cleaned up because there were a handful of cases where the analysis failed to converge and misplaced data points. These degenerate data points are deleted without much consequence because interpolation can patch up the missing data point.
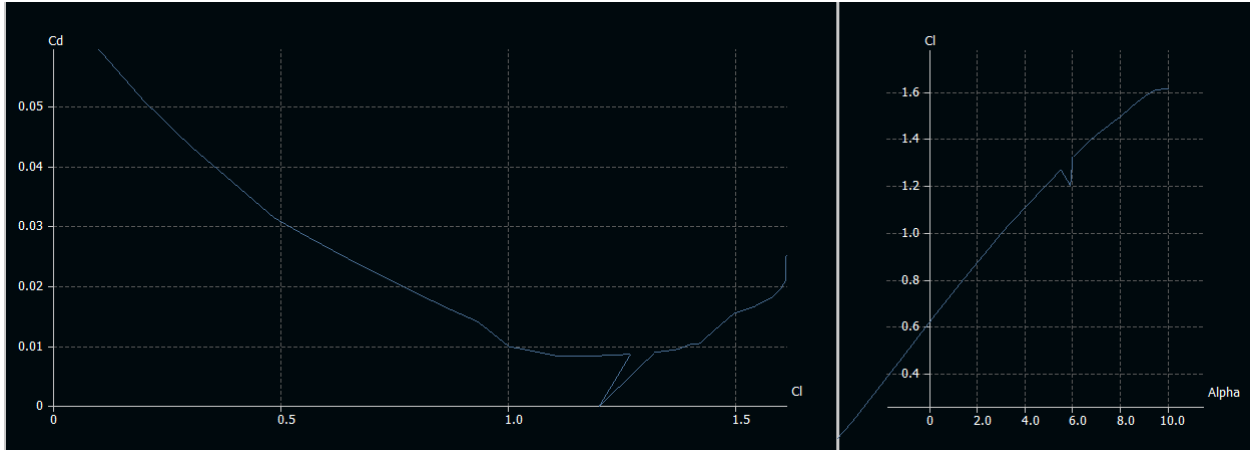
Figure 4: Example of erroneous data point

Once the data is cleaned up and in Excel, the final post-process is to calculate the change in coefficient of lift due to angle of attack. In a perfect world, employing a finite difference formula should accurately show how $C_{L,alpha}$ varies with angle of attack, but some combinations of airfoils and Reynold numbers create curves that are not perfectly smooth, and the sensitivity of a 2-point stencil finite difference would produce unrealistic results. The solution was to still use a 2-point finite difference to find the slopes, but then to take the median of all of the slopes to get an effective $C_{L,alpha}$. This works due to the linearity of most C_L vs angle of attack relationships but starts to break down at more extreme angles of attacks and edge cases.

3.2 Chosen Airfoil Specifications

The airfoils were one of the randomly varied parameters in the Monte Carlo optimization process. The final aircraft design ended up using the GOE 448 profile for the wing. Additionally, the NACA 0012 profile was used for the vertical and horizontal stabilizers (this was not randomized). Compared to the other candidates, the GOE 448 is on the thicker size and has the largest $C_{L,alpha=0}$.

13
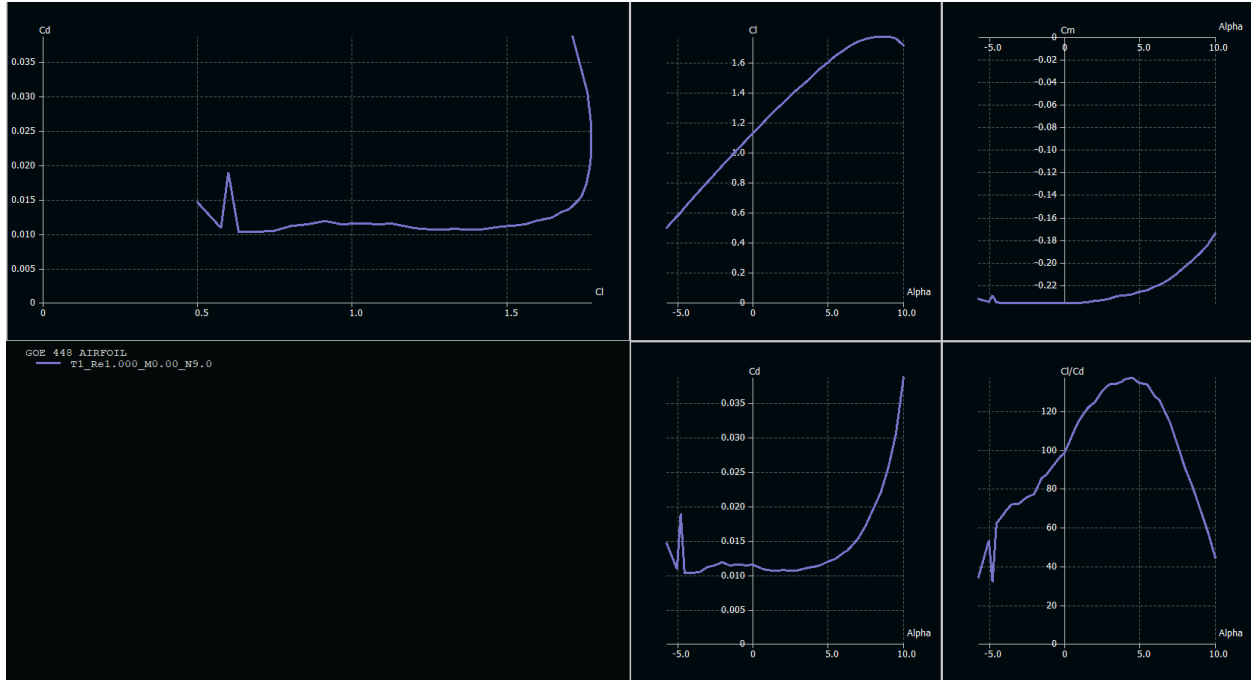
Figure 5: Relevant polars for GOE 448 at Re = 1e6

The little spike that can be seen on all of the polars can be attributed to a single corrupt data point, which was removed prior to the airfoil data being imported into MATLAB. During the later stages of optimization, a trend that occurred was this airfoil started to produce the most number of aircraft that was able to meet all of the design requirements.

3.3 Total Aircraft Drag

The total drag for each aircraft configuration is estimated with the component build-up method. This involves calculating the coefficient of drag for each component x on the aircraft ($C_{D,x}$) and deriving the total drag coefficient (C_D) from the individual contributions. The individual and total drag coefficient is the combination of two forms of drag: parasitic ($C_{D,0}$) and induced ($C_{D,i}$).

$$C_D = C_{D,0} + C_{D,i}$$

These two subdivisions can also be thought of as the drag without the presence of lift and the drag due to lift.

The parasitic drag associated with each component is the drag caused by that component's skin friction and form drag as well as the interference drag between any two intersecting components. The parasitic drag is very sensitive to changes in the boundary layer close to the component surface. The boundary layer geometry and behavior are determined by the local Reynold's number, and thus the parasitic drag is sensitive to changes in velocity and length of the component.

The induced drag is a measure of the drag caused by lift produced by each aerodynamic surface, specifically the component of the lift vector which points in the direction of drag. The induced drag for each component is proportional to the square of the coefficient of lift for each component. The coefficient of lift is inversely proportional to the size of the component assuming a constant velocity and weight. Thus, as the size of the component increases, the induced drag decreases. The induced drag coefficient is also inversely proportional to the aspect ratio of the aerodynamic surface.

Our optimization process produced an aircraft with a relatively large wing and low aspect ratio. This is most likely due to a few factors in concert. First, the structural weight savings of a low aspect ratio wing: the same size wing with a higher aspect ratio will have its center of gravity further from the root, meaning the bending moment is larger for the same sized wing, which necessitates more structural weight to support the extra load. Second, the pressure drag savings from increased turbulent flow: laminar flow can lead to an adverse pressure gradient that increases drag, and a larger chord length ensures more turbulent flow over the wing.

Our mission coverage and endurance requirements produce a high cruise altitude. Thus, we never approach the critical Mach number of drag divergence. Therefore, we have optimized our aircraft for a low-to-medium speed drag configuration.
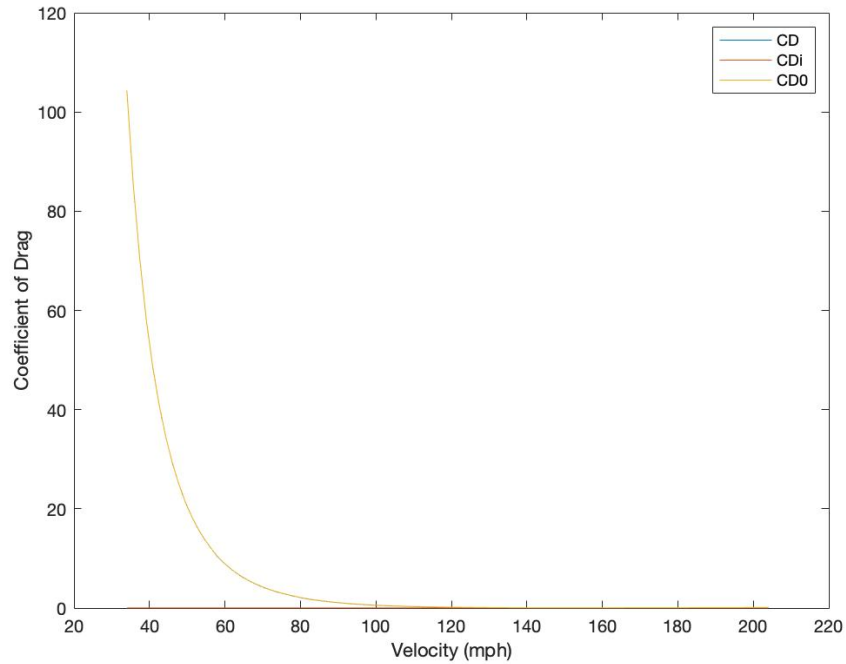
Figure 6: Coefficient of Drag vs velocity.

The plot above illustrates how our configuration is most affected by parasitic drag. Note that 200 miles per hour corresponds to about Mach 0.3. Thus we are flying very slowly at this altitude and have not yet reached the point at which induced drag plays its biggest role.

3.4 Stability

The derived aircraft stability coefficients can be seen in Table 5.

Table 5: Stability Coefficients

Name	Final Aircraft Value	RQ-2 Pioneer Value	Unit	Calculated From:
CL0	1.13	0.385	-	XFLR5
CL_a	3.5956	4.78	/rad	MATLAB
CL_adot	0.3010	2.42	/rad	MATLAB
CL_q	1.009	8.05	/rad	DATCOM
CL_de	0.2881	0.401	/rad	MATLAB
CD0	0.0188	0.06		MATLAB
CD_a	1.3191	0.43	/rad	MATLAB
CD_de	0.1057	0.018	/rad	MATLAB
Cm0	-0.2338	0.194		MATLAB
Cm_a	-5.6701	-2.12	/rad	MATLAB
Cm_adot	-2.4124	-11	/rad	MATLAB

16

Cm_q	-6.5758	-36.6	/rad	MATLAB
Cm_de	-0.1801	-1.76	/rad	MATLAB
CY_beta	-0.2459	-0.819	/rad	DATCOM
CY_p	0.1457	-	/rad	DATCOM
CY_dr	-	0.191	/rad	did not model rudder
Cl_beta	-0.1294	-0.023	/rad	DATCOM
Cl_p	-0.276	-0.45	/rad	DATCOM
Cl_r	0.1233	0.265	/rad	DATCOM
Cl_da	-	-0.161	/rad	did not model aileron
Cl_dr	-	-0.00229	/rad	did not model rudder
Cn_beta	0.01748	0.109	/rad	DATCOM
Cn_p	-0.0319	-0.11	/rad	DATCOM
Cn_r	-0.02871	-0.2	/rad	DATCOM
Cn_da	-	0.02	/rad	did not model aileron
Cn_dr	-	-0.0917	/rad	did not model rudder

To calculate the stability derivatives, both MATLAB and DATCOM were used. The coefficients that were calculated in MATLAB used equations from Chapter 3 of Nelson's "Flight Stability and Automatic Control."

```
 1  BUILD
 2   $FLTCON  NMACH=1.0, MACH(1)=0.2117,
 3    NALPHA=10.0, ALSCHD(1)=-20.0,-12.0,-8.0,-4.0,-2.0,0.0,2.0,4.0,8.0,12.0,
 4    NALT=1.0, ALT(1)=62000.0, WT=1107.0,
 5    RNNUB(1)=1.4065E5$
 6   $SYNTHS XCG=5.6269, ZCG=0.0, XW=1.752, ZW=0.95, ALIW=0.0, XH=9.543,
 7    ZH=2.0, ALIH=0.23, XV=9.354, ZV=1.4$
 8   $OPTINS SREF=150.0$
 9   $BODY NX=4.0,
10     X(1)=0.0,0.25,11.75,12.0,
11     S(1)=0.1,6.15,6.16,0.1$
12  NACA-W-4-9413
13   $WGPLNF CHRDTP=7.0, SSPNE=10.725, SSPN=10.725,
14    CHRDR=7.0, SAVSI=0.0, CHSTAT=0.25,
15    TWISTA=0.0, DHDADI=0.0, DHDADO=0.0, TYPE=1.0$
16  NACA-H-W-0012
17   $HTPLNF CHRDTP=1.243, SSPNE=8.2133, SSPN=8.2133, CHRDR=1.826, SAVSI=0.0,
18    CHSTAT=0.25, TYPE=1.0$
19  NACA-V-W-0012
20   $VTPLNF CHRDTP=2.319, SSPNE=5.8, SSPN=5.8, CHRDR=2.586, SAVSI=0.0,
21    CHSTAT=0.25, TYPE=1.0$
22  CASEID ----- MAE 154A Group 4 -----
23  SAVE
24  DAMP
25  DERIV RAD
26  NEXT CASE
```

Figure 7: DATCOM Inputs

DATCOM is a software developed by McDonnell Douglas and the U.S. Airforce in the late 70s. It is capable of calculating values based relevant to stability and control for complex aircraft geometry.

All of the stability derivatives of the final aircraft are at most an order magnitude away from its counterpart in the Pioneer. There is a sign change in $C_{m,0}$. The moment coefficient at zero angle of attack is negative, meaning that the airplane trims at a negative angle of attack. A general trend is that the majority of the stability coefficients are smaller for this aircraft than for the RQ-2. This implies that the will be both less maneuverable than the RQ-2 and more resilient to small perturbations in flight.

4. Propulsion

4.1 Propeller Selection

The propeller for our aircraft was selected by placing the highest emphasis on high altitude performance. Thus, the 54H60 propeller system, the same one used on the AC-130 and Lockheed P-3 Orion (two aircraft with service ceilings over 55k feet), was selected for our aircraft. This propeller system is ideal for its proven high-altitude capability and fully adjustable blade angle. This allows our aircraft to operate under conditions as close to ideal (cruise) as possible throughout the velocity range.

Figure 8: The 54H60 propeller system seen operating on the AC-130.

The efficiency of the propeller system is estimated by assuming that the efficiency characteristics are the same as those described in figure 13.12 in the Raymer text. This simplification will lead to some differences from physical reality due to differences in number of

blades, activity factor, and blade design C_L. Because our propeller is selected for the physical

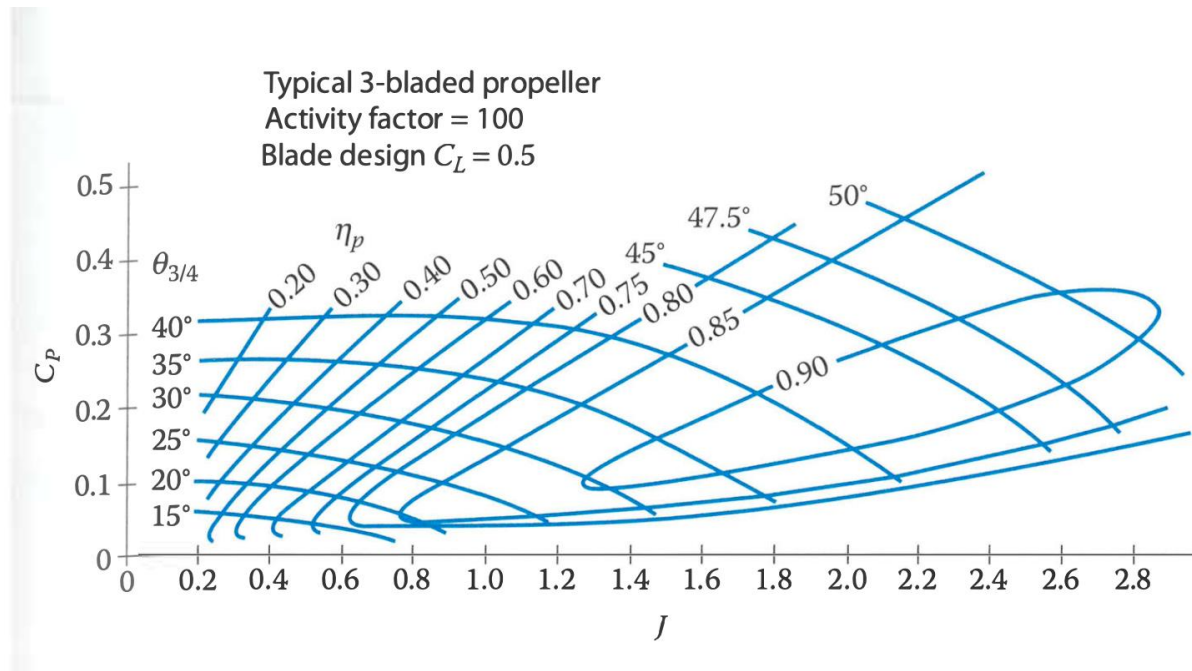realities of the mission, we can still be confident in our propeller selection and thrust results.

Figure 9: Efficiency curves used to design the propulsion system, figure 13.12, Raymer.

At our chosen cruise velocity of 140 mph, our cruise altitude is 61,890 ft. At this altitude,

the coefficient of power, $c_P = \frac{P_{eng}}{\rho n^3 D^5}$, is approximately 0.33. This value is constant at a given

altitude, and so the efficiency of the propeller depends solely on the advance ratio, and therefore

forward speed, of the aircraft, assuming fully adjustable propeller blade angle, as is the case for

the 54H60. Therefore, we find that the propeller efficiency varies with forward speed as follows.

Table 6: Table of velocity and propeller efficiency with blade angles.

Velocity (mph)	η_{pr}	Blade Angle
$0 - 50$	0.2	40°
$50 - 68$	0.3	40°
$68 - 87$	0.4	40°
$87 - 106$	0.5	40°

106 – 121	0.6	40°
121 – 140	0.7	40°
140 – 156	0.75	45°
156 – 163	0.8	45°
163 - 200	0.85	45°
200+	0.9	47.5°

4.2 Engine Selection

The selection of the engine for this design was made primarily on the basis of the required power/thrust at various altitudes (particularly cruising altitude), and the engine's capability to match these requirements. A table of engine candidates is seen below in Table 7.

Table 7: Engine Candidates

Engine	weight (lb)	SFC (lb/(hp-hr))	RPM	Largest width/ depth	gear ratio (1:)	power output (hp)
Rotax912	132.3	0.468516	5500	1.89	2.273	79.9
TAE125	337.3	0.319	3900	2.68	1.689	130.1
Rotax914	172	0.454	5800	1.89	2.273	100
HKS700E	121	0.45	5800	2.5	2.58	56
O300	268	0.331	2700	2.635	1	145

The final engine selection was the Rotax 912. It was one of the lightest options, because we found that our power expectations were greater than reality after downsizing our aircraft significantly through the optimization process.
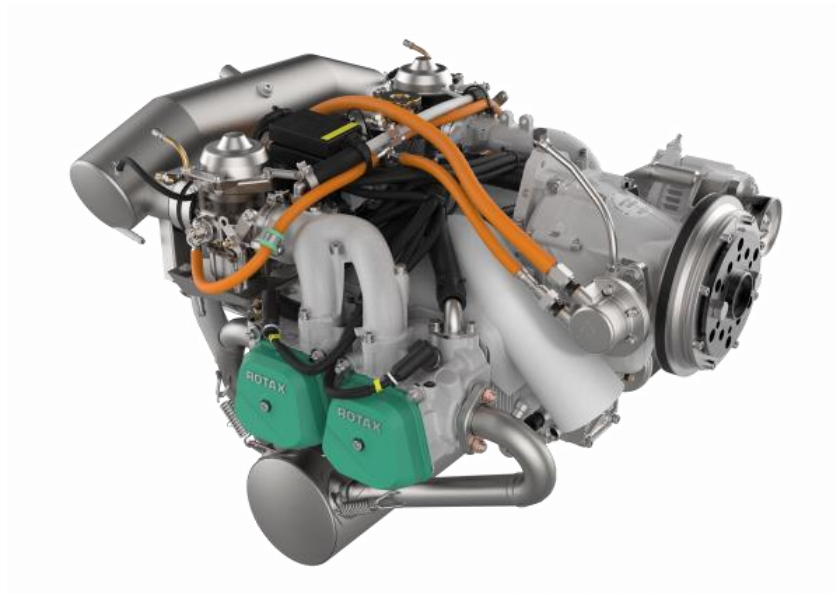

Figure 10: Rotax 912 Engine

4.2.1 Power/ Thrust Curves

The selection of our engine and propeller allows us to find the power available for our configuration. Using the power output by the engine and the propeller efficiency described in the sections above, we can calculate the power available at each velocity. The power required at each velocity is the product of the drag at each velocity (outlined in section 2) multiplied by the velocity in question. Thus, power available and power required curves can be derived for each configuration. The power required and power available for our final aircraft is displayed below.
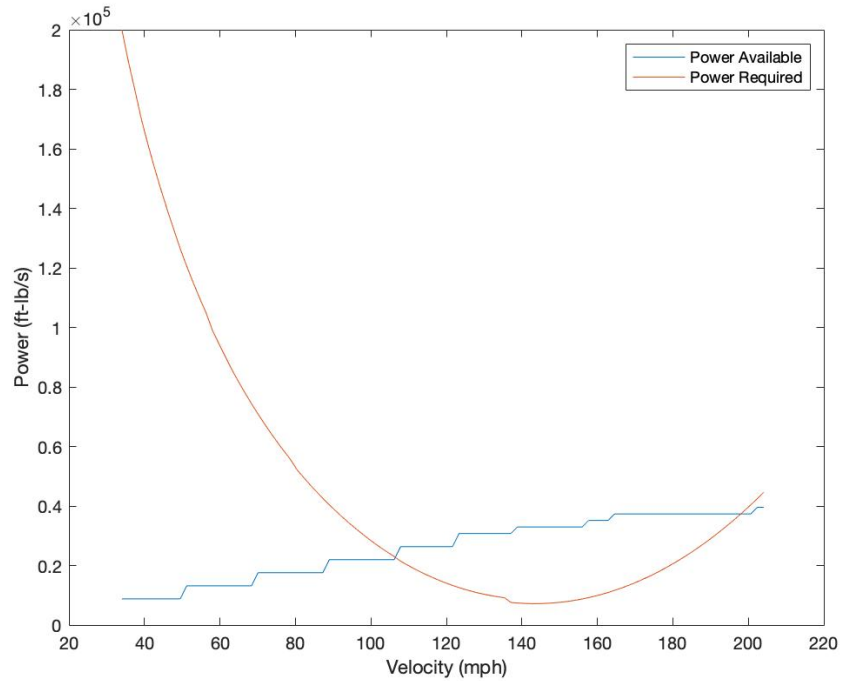
Figure 11: Power available and power required for our final aircraft configuration.

5. Guidance Navigation, and Control

5.1 Simulation Global Plans

The purpose of the flight simulation is to act as a global and local planner, deciding on trajectories and sending determined attitude, altitude, and velocity setpoints to the lower-level autopilot and developed dynamics simulation. In this way, the simulation acts as a flight controller acting on feedback from a simulated plant instead of a physical system.

The global planner and local planner in the simulation are both combined into the "waypoint guid" block, which is meant to control the actions of the simulation through four distinct flight modes. The first and most trivial, gain altitude mode has the plane circle in a safe location as it gains altitude to its survey cruise altitude. The second is a waypoint following mode which travels through a set of hard-coded waypoints meant to cover the entirety of Angeles National Forest (a map of which is seen below in Figure 12). The third flight mode

directs the plane to travel to a known fire location, and then loiter above at a given altitude upon reaching the fire. The final mode is a return to home mode which navigates the plane back to the home airfield and terminates the simulation upon satisfying three checks: distance from home, altitude error, and velocity error.
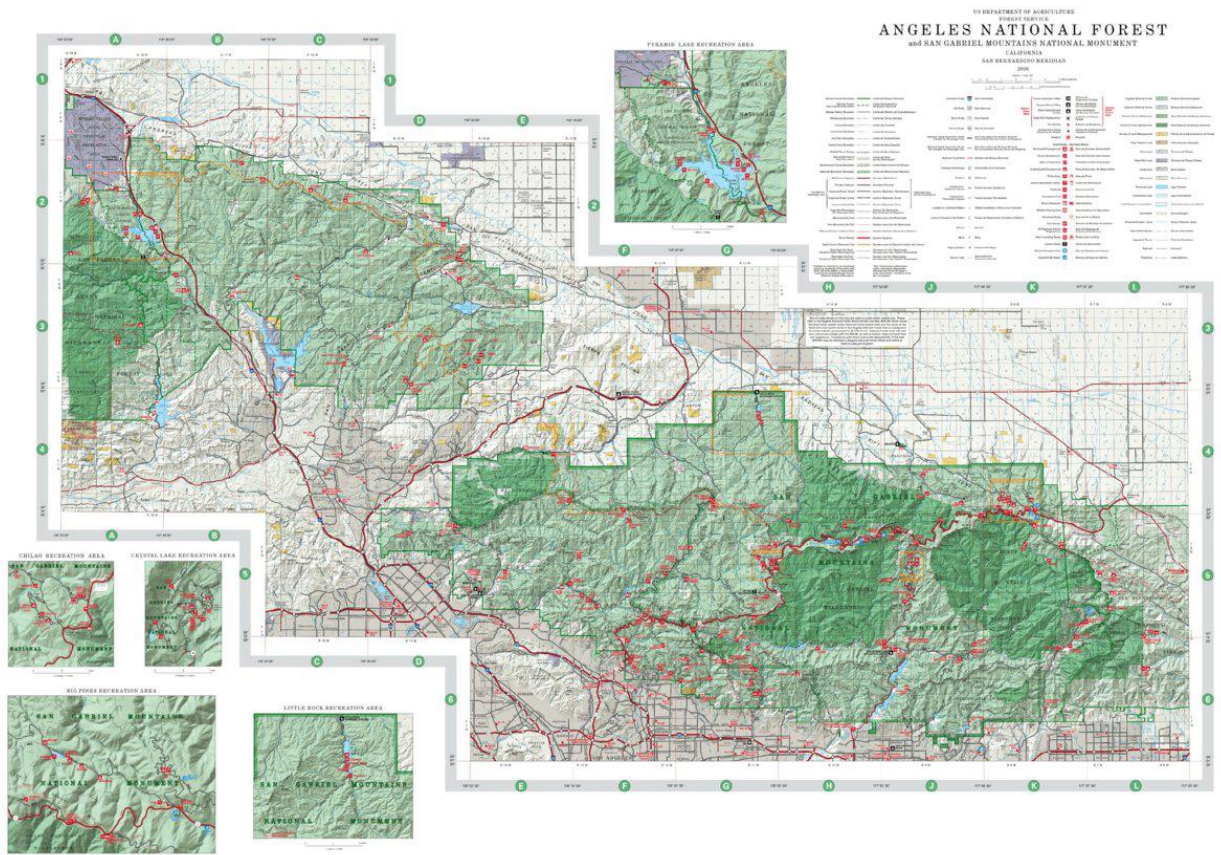

Figure 12: Map of Angeles National Forest

5.2 Modifications from Original Model

For this project, a premade Simulink autopilot simulation was provided. A modified version of the provided Simulink model is seen in Figure 13.
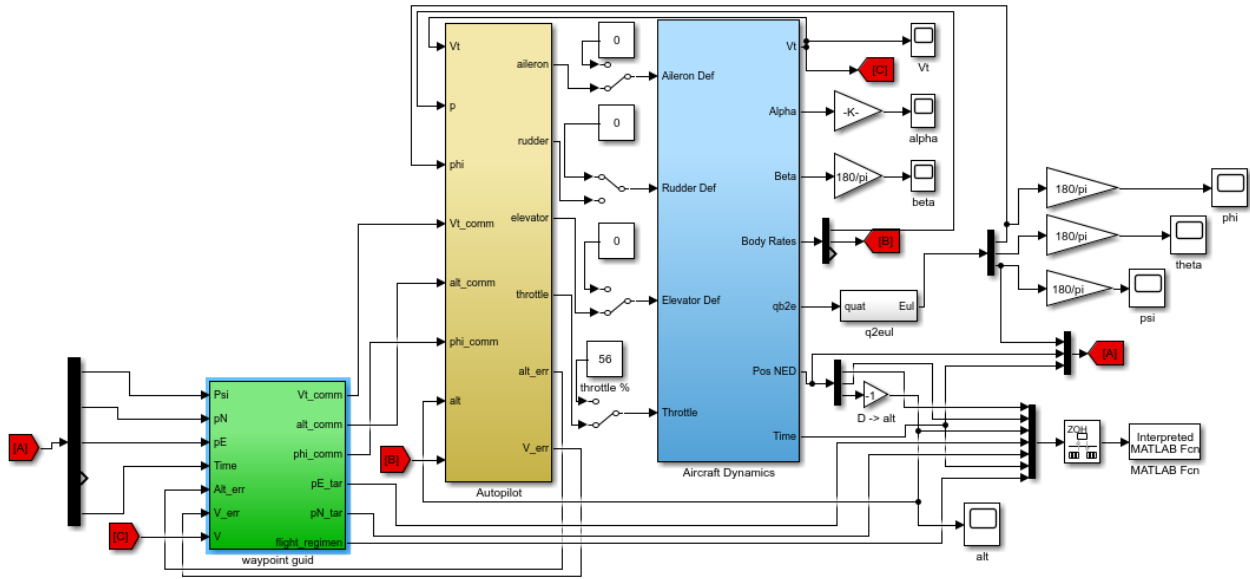
Figure 13: Modified Autopilot Block Diagram

As stated in 5.1, most modifications were made to the "waypoint guid" block. Some notable modifications were also made to the draw map function, which allowed for the position, coverage, and waypoint location to be plotted over the map of Angeles National Forest, as well as adding feedback lines for altitude and velocity error back into the planner block.

Apart from the mentioned altitude and velocity error feedback inputs, the planner block also received time and velocity inputs from the aircraft dynamics block. Additional outputs specifying velocity and altitude setpoints were fed into the autopilot block, and a flight mode tracker was fed from the planner to the map drawing function to add visual clarity on which flight mode was running at any given time.

The waypoint guide function had several key functionalities added. The first addition of note is the process of deciding flight modes. Each of the four previously discussed flight modes had triggers which would start or end it, it is important to note however that the fire detection and travel home triggers are arbitrarily set to happen after a given amount of time. In a realistic system, these would be additional inputs.

25

For the waypoint travelling mode, a set of hard-coded waypoints were written. A possible improvement on this planner would be accepting the flight conditions and swath width of the thermal sensor to create an optimized set of waypoints to follow. The modified waypoint guide block is seen below in Figure 14.
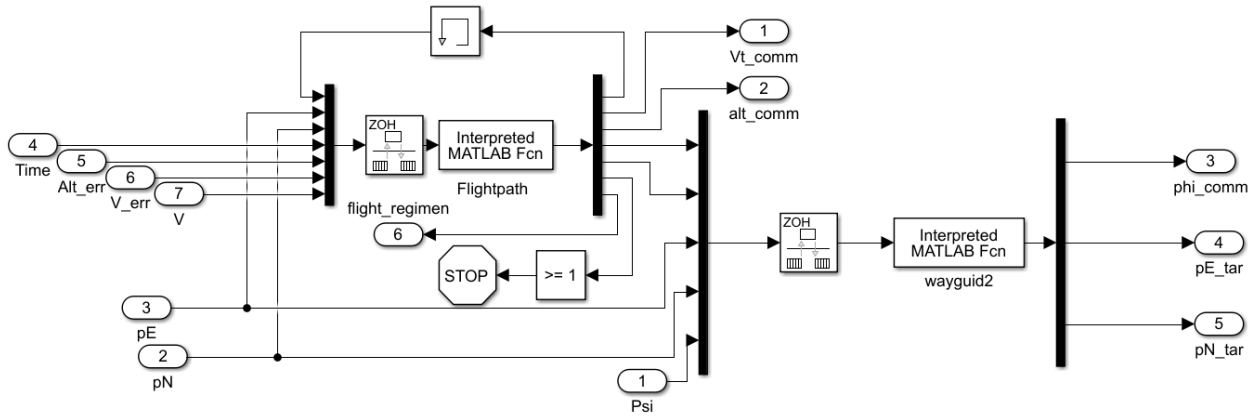

Figure 14: Modified Waypoint Guide Function

Most of the inputs are now fed through the flightpath function, which incorporates the logic of switching between flight modes, contains the hardcoded waypoints, and directly feeds velocity and altitude setpoints to the autopilot based on aircraft design determined values. For example, when travelling through waypoints, the flightpath function outputs velocity and altitude setpoints of the ideal cruise conditions, approximately 140 miles per hour and 60,000 feet respectively. The waypoint targets are fed to wayguid2 along with current positions to generate attitude setpoints for the autopilot. The final purpose of the flightpath function is to determine when to end the simulation, based on landing criteria being met or not.

6. Design Optimization

The aircraft was optimized for the minimum weight case that can still meet the requirements listed in (1.2) by applying the Monte-Carlo approach. Our approach involves accepting viable aircraft parameters and randomly varying them within a certain range centered around the

original parameter. The combination of these random inputs then forms a unique configuration.

Each configuration's performance parameters are calculated and compared to the mission

requirements. Configurations which pass all requirement, lift, and stability checks are considered

to be viable aircraft. The weight of each viable configuration is saved, along with the random

values generated for each component. The total weight can then be plotted against the size of

each individual parameter. The resulting plots are analyzed for trends, and the initial inputs are

adjusted according to the trends identified. This process is outlined in the figure below.
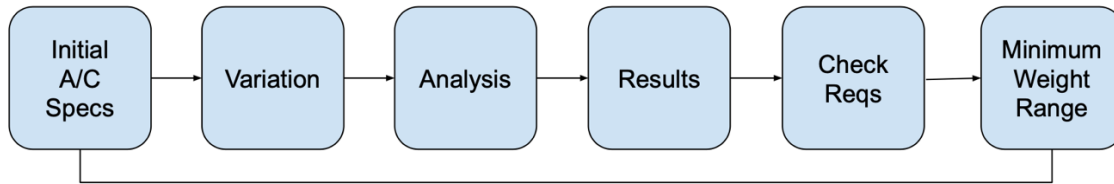

Figure 15: Optimization process implemented post-PDR.

The optimization process made it plain that our viable aircraft produced for the PDR was

substantially too large for the mission requirements. All of the aircraft we had surveyed and

identified as viable design outlines were designed to carry significant payloads, while our aircraft

has a very lightweight payload. Thus, as illustrated in the figure below, the fifth run of the

optimization process clearly shows room to decrease the size and weight of all important inputs –

fuel weight, wing, and tail area. Note that in any plot with velocity as the dependent variable, a

vertical line appears at V = 133 mph. This is because this velocity corresponds to an altitude of

over 85,000 ft in order to meet the coverage requirements of the mission. Because the

characteristics of flying at high altitude are already simplified by our model, we chose this as the
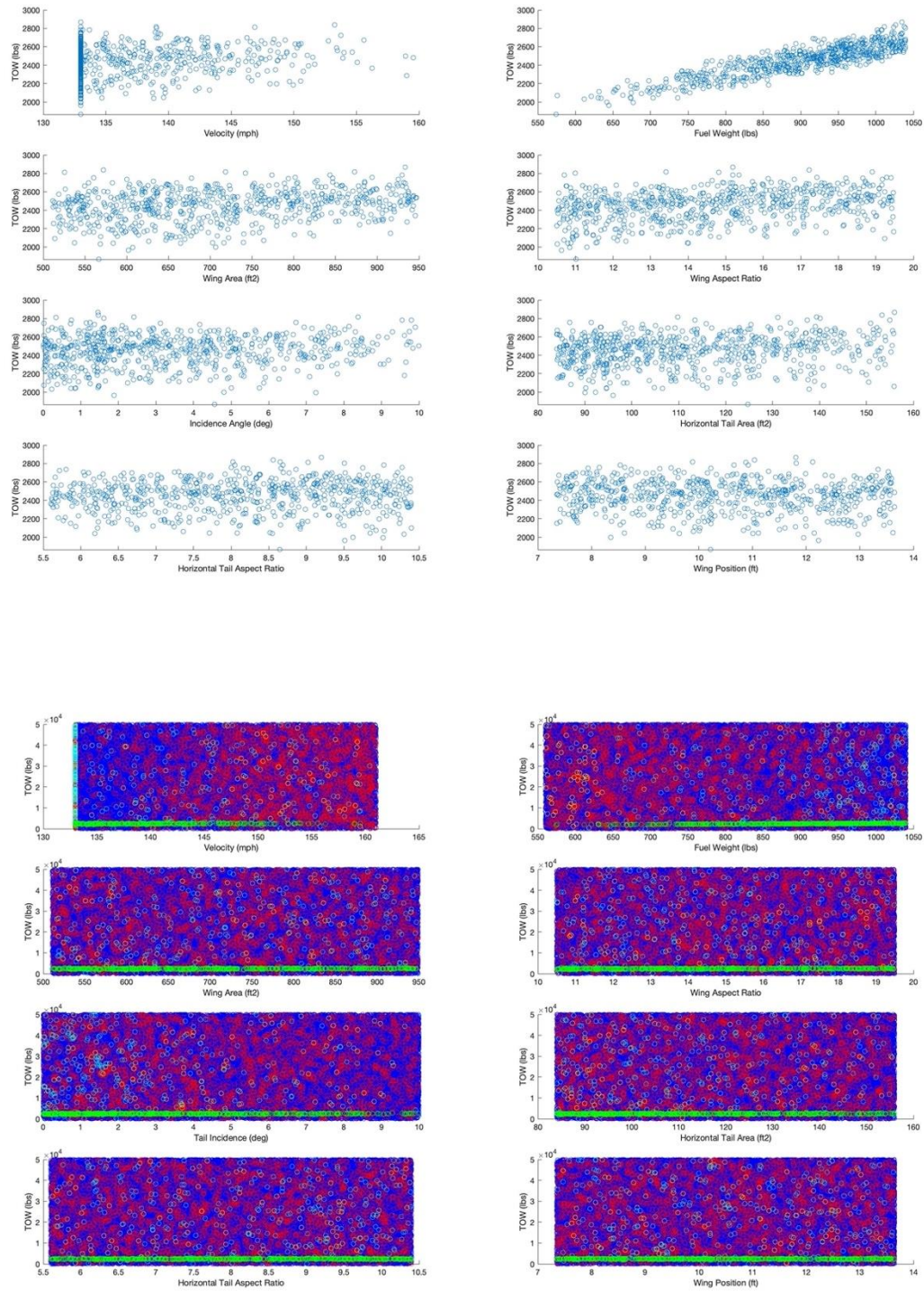
maximum altitude our process would test.

27

Figure 16: All viable aircraft (top) and all aircraft (bottom) produced by the fifth run of the Monte-Carlo approach.

The graph above displays all aircraft produced by the first run of the Monte-Carlo approach. The top graphs, with all blue markers, indicate the viable aircraft produced, and the bottom graphs, with multicolored markers, indicate all the aircraft produced. In the colorful figure, each marker indicates a different fail or pass condition. The blue markers indicate the configuration failed due to power required being greater than power available at cruise in either the full or empty fuel arrangement, the red markers indicate the configuration failed due to available endurance not exceeding required endurance, the yellow markers indicate the aircraft's lift did not exceed or match its weight in cruise conditions, the black markers indicate the aircraft did not meet climbing requirements, and the cyan markers indicate the configuration did not meet minimum turn radius requirements. Green markers indicate viable aircraft.

Obvious trends are present in the fuel weight and wing and tail area graphs. This indicated that our plane was overdesigned, and the scale of the design could be reduced. This was accomplished by slowly reducing the wing and tail area, as well as the fuel weight, over the next several runs. As our weight estimate became more refined and more configurations became viable, a trend was revealed in the incidence angle graph, prompting us to reduce the input incidence angle.
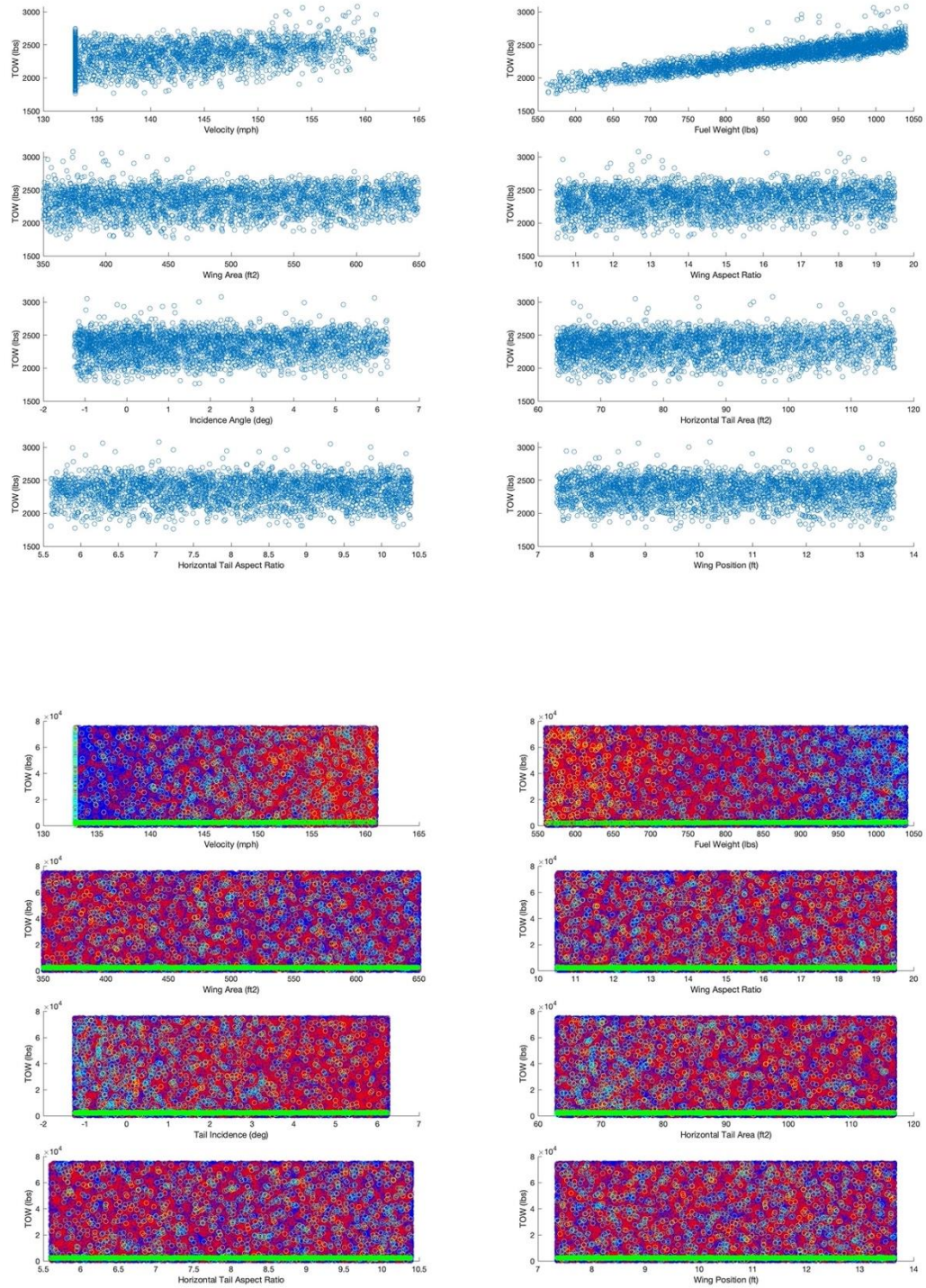
Figure 17: All viable aircraft produced by the eighth run of the Monte-Carlo approach.

The second graph from the bottom on the left side of the figure above shows the trend in the incidence angle. Usually, a large amount of viable configurations relative to the number tested are required to pass in order to identify trends in the graphs. For this reason, we decided to try to obtain the minimum fuel weight, wing and tail area required before optimizing the positions of the components. This was attempted in order to make trends more obvious with less runs. The figure below displays the graphs produced for the last optimization run and includes new graphs displaying the position of each component against total takeoff weight.
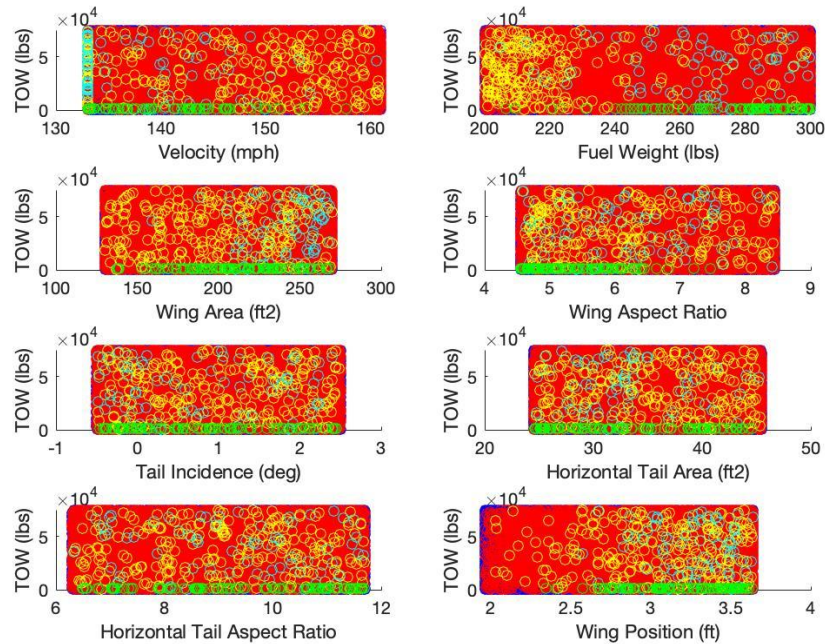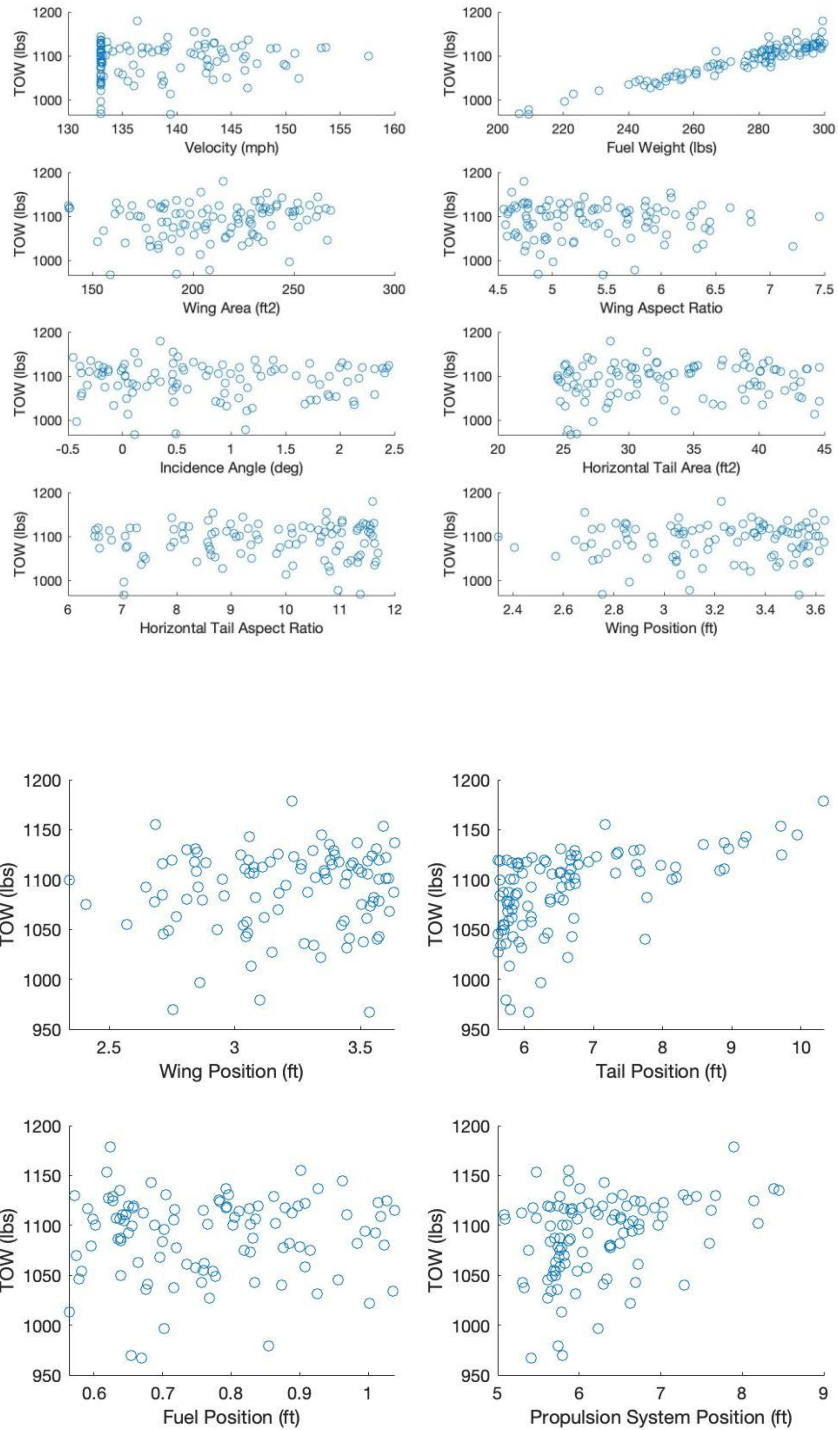
Figure 18: *All aircraft produced by the 19ᵗʰ and final run of the optimization process.*

The graphs above indicate clear minima surrounding the wing and tail area, as well as

obvious trends in the tail and propulsion system positions. The minimum weight case for this run

was taken and used as the viable aircraft. This decision is supported by the plot of viable aircraft percentage against run number and total aircraft weight against run number.
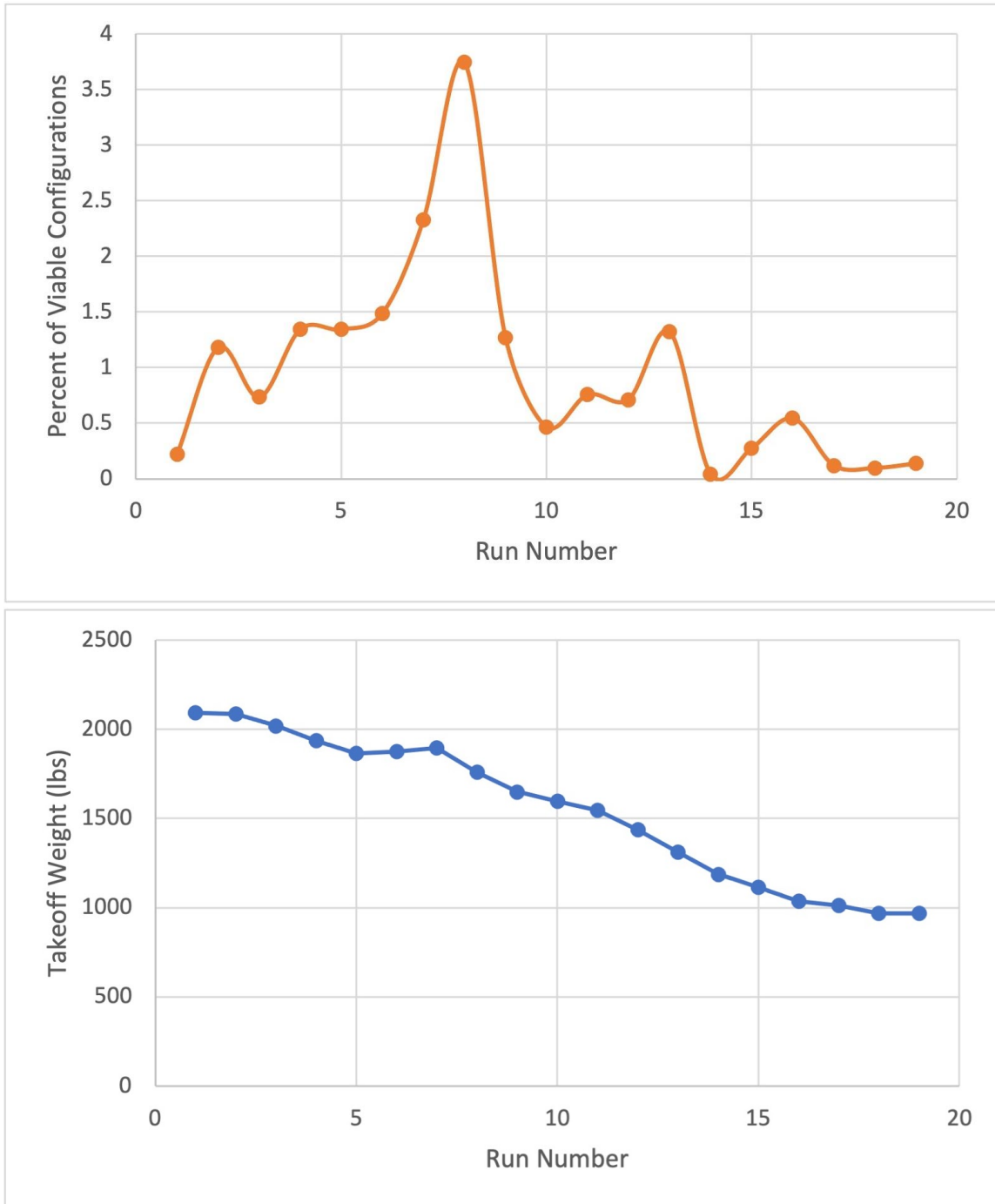

Figure 19: Percent of viable configurations and total takeoff weight against run number for the Monte-Carlo process.

The figure above illustrates that by steadily decreasing the fuel weight and size of aerodynamic surfaces, the takeoff weight was reduced until only minimal changes were achieved.

7. Conclusion

The goal of this project was to design a UAV which could meet aggressive endurance and coverage requirements. Fire detection and prevention are tough challenges which must be solved with increasing global temperatures and wildfires continued effects on Southern California.

Through the design process, our team was able to implement many of the lessons from previous classes and create a first iteration UAV design. We faced several challenges and found several flaws in our final results. Taking on such a high altitude mission presented several unexpected challenges, and we ultimately were not able to account for all of them. Despite the flaws, we are incredibly proud of our work and appreciative of the chance to work and learn in this class. Much thanks goes to Professor Toohey for guiding us through the design and excellent instruction in MAE 154A and S.

8. References

[1] cspropeller.com. (2016). *54h60 Propeller System.* Retrieved from https://cspropeller.com/2016/08/16/54h60-propeller-system/

E. Hartman, D. B. (1938). *The Aerodynamic Characteristics of Full-Scale Propellers Having 2, 3, and 4 Blades of Clark Y and R.A.F. 6 Airfoil Sections.*

McDonnell Douglas Astronautics Company. (1976). *THE USAF STABILITY AND CONTROL DATCOM.*

R. Wilkinson, R. B. (2015). *Liquid Cooled Turbocharged Propulsion System for HALE Application.*

Raymer, D. (1989). *Aircraft Design: A Conceptual Approach.*

Scholz. (n.d.). *Aircraft Design, Chapter 13 - Drag Prediction.*

Neslson, R. (1998). *Flight Stability and Automatic Control*